

Article

Solar-Driven Syngas Production Using Al-Doped ZnTe Nanorod Photocathodes

Youn Jeong Jang ^{*}, Chohee Lee, Yong Hyun Moon and Seokwoo Choe

Department of Chemical Engineering, Hanyang University, Seongdong-gu, Seoul 04763, Korea; chgml9612@hanyang.ac.kr (C.L.); myh4791@hanyang.ac.kr (Y.H.M.); choe5192@hanyang.ac.kr (S.C.)
^{*} Correspondence: yjang53@hanyang.ac.kr; Tel.: +82-2-2220-0526

Abstract: Syngas, traditionally produced from fossil fuels and natural gases at high temperatures and pressures, is an essential precursor for chemicals utilized in industry. Solar-driven syngas production can provide an ideal pathway for reducing energy consumption through simultaneous photoelectrochemical CO₂ and water reduction at ambient temperatures and pressures. This study performs photoelectrochemical syngas production using highly developed Al-doped ZnTe nanorod photocathodes (Al:ZnTe), prepared via an all-solution process. The facile photo-generated electrons are transferred by substitutional Al doping on Zn sites in one-dimensional arrays to increase the photocurrent density to -1.1 mA/cm^2 at $-0.11 \text{ V}_{\text{RHE}}$, which is 3.5 times higher than that for the pristine ZnTe. The Al:ZnTe produces a minor CO (FE $\approx 12\%$) product by CO₂ reduction and a major product of H₂ (FE $\approx 60\%$) by water reduction at $-0.11 \text{ V}_{\text{RHE}}$. Furthermore, the product distribution is perfectly switched by simple modification of Au deposition on photocathodes. The Au coupled Al:ZnTe exhibits dominant CO production (FE $\approx 60\%$), suppressing H₂ evolution (FE $\approx 15\%$). The strategies developed in this study, nanostructuring, doping, and surface modification of photoelectrodes, can be applied to drive significant developments in solar-driven fuel production.

Keywords: photoelectrochemical; CO₂ reduction; syngas; ZnTe; nanorod; photocathode



Citation: Jang, Y.J.; Lee, C.; Moon, Y.H.; Choe, S. Solar-Driven Syngas Production Using Al-Doped ZnTe Nanorod Photocathodes. *Materials* **2022**, *15*, 3102. <https://doi.org/10.3390/ma15093102>

Academic Editor: Leszek Zaraska

Received: 31 March 2022

Accepted: 21 April 2022

Published: 25 April 2022

Publisher's Note: MDPI stays neutral with regard to jurisdictional claims in published maps and institutional affiliations.



Copyright: © 2022 by the authors. Licensee MDPI, Basel, Switzerland. This article is an open access article distributed under the terms and conditions of the Creative Commons Attribution (CC BY) license (<https://creativecommons.org/licenses/by/4.0/>).

1. Introduction

Synthetic gas (syngas), a mixture of carbon monoxide (CO) and hydrogen gas (H₂), is an essential precursor for the production of hydrocarbon fuels and value-added chemicals, such as alcohols and acetic acid [1,2]. Industrial syngas is typically produced from fossil fuels and natural gases at high temperatures and pressures [3,4]. However, employing photoelectrochemical (PEC) water and CO₂ reduction at ambient temperatures and pressures is a sustainable and environmentally friendly alternative to traditional syngas production [5,6].

PEC cells comprising semiconductor photoelectrodes can harvest solar energy to perform electrochemical catalytic reactions [7–9]. The standard reduction potential of CO₂ to CO (CO₂ + 2H⁺ + 3e⁻ → CO + H₂O, E_o = $-0.11 \text{ V}_{\text{RHE}}$) is slightly more negative than that of water to H₂ (2H⁺ + 2e⁻ → H₂, E_o = $0.0 \text{ V}_{\text{RHE}}$). Therefore, ideally, any photocathode can be used in photoelectrochemical CO₂ reduction to produce H₂ in a thermodynamic manner. Moreover, CO₂ to CO conversion is kinetically poorer than water-to-H₂ conversion, primarily because of the slow CO₂ adsorption and intermediate formation [10–12]. This indicates that direct syngas production can be achieved using a single photoelectrochemical CO₂ reduction system. Furthermore, the ratio of H₂/CO, which is the key factor determining the upgraded product selectivity, is controllable by catalysts [13–15].

ZnTe semiconductors are an interesting and useful class of photoelectrocatalysts and have received considerable attention owing to their narrow bandgap energy (2.26 eV) and band alignment. This allows harvesting of visible light and a suitable band alignment for syngas production. Specifically, the conduction band minimum (CBM) of ZnTe located at

$-1.63 V_{\text{RHE}}$, which is highly negative compared to CO_2 -to- CO reduction potential, can provide a strong driving force for photoexcited electron injection for syngas production [16–18]. However, ZnTe photocathodes typically exhibit poor photoexcited charge separation because of the rapid charge recombination and kinetically inactive catalytic reaction [16,19].

Therefore, this study proposes Al-doped ZnTe nanorod photocathodes for photoelectrochemical syngas production. The one-dimensional array ZnTes can provide a shortened carrier transport distance, which can facilitate their separation. Furthermore, ZnTes with substitutional Al dopants at Zn sites exhibit increased charges transport activity in the bulk compared with pristine ZnTe. The difference in valence states between Al (Al^{3+} in lattice) and Zn (Zn^{2+} in lattice) causes a significantly increasing major carrier concentration. In addition, PEC syngas production is demonstrated, enabling a change of the H_2 :CO ratio from 5:1 to 1:4, using surface-modified ZnTe-based photocathodes. The proposed method results in a significant enhancement in syngas production and H_2 /CO ratio changes. The photocathode preparation, results, and effects of catalyst modification are presented in this paper.

2. Materials and Methods

2.1. Materials

Fluorine doped tin oxide substrate was purchased from Pilkington, Lancashire, UK. $\text{Zn}(\text{NO}_3)_2 \cdot 6\text{H}_2\text{O}$ (99%), ammonia water (28–30%), $\text{Al}(\text{NO}_3)_3 \cdot 9\text{H}_2\text{O}$ (98%), Na_2TeO_3 (99%), NaBH_4 (99%) were purchased from Aldrich, Burlington, MA, USA. KHCO_3 (99.7%) was purchased by Junsei chemicals, Tokyo, Japan. All chemicals used in this work were as received, without further purification.

2.2. Synthesis of Al Doped ZnTe Nanorod Film

Al-doped ZnTe nanorods were prepared using the following two steps. First, the Al doped ZnO nanorods were solvothermally grown on a ZnO (50 nm)-sputtered fluorine-doped tin oxide substrate (FTO, PECTM 8/Pilkington, Lancashire, UK) in an aqueous solution containing 10 mM $\text{Zn}(\text{NO}_3)_2 \cdot 6\text{H}_2\text{O}$ (Aldrich, Burlington, MA, USA), ammonia water (28–30%, Aldrich, Burlington, MA, USA), and $\text{Al}(\text{NO}_3)_3 \cdot 9\text{H}_2\text{O}$ (Aldrich, Burlington, MA, USA) at 95 °C for 2 h [19,20]. The concentration of Al precursors was adjusted to 0, 1, 3, and 5 atomic % against the concentration of Zn precursors, and the samples were named as Al:ZnO x , where $x = 0, 1, 3, \text{ and } 5$, respectively. Then, Al doped ZnTe nanorods were prepared from Al-doped ZnO nanorods using the previously reported anion exchange reaction in an aqueous solution containing 0.45 mM Na_2TeO_3 (Aldrich, Burlington, MA, USA) and 26.5 mM NaBH_4 at 95 °C for 2 h [16]. Because the Al dopant concentration in ZnTe corresponds to the concentration in ZnO, Al-doped ZnTe nanorod samples were named Al:ZnTe X , where $X = 0, 1, 3, \text{ and } 5$, respectively.

2.3. Physico and Chemical Characterizations

The crystal structures of Al-doped ZnO and Al-doped ZnTe were examined using X-ray diffraction (XRD) (Mac Science, Kanagawa, Japan, M18XHF using Cu K α radiation, $\lambda = 0.15406$ nm). The morphologies of the electrodes were investigated using field-emission scanning electron microscopy (FESEM) (JEOL, Tokyo, Japan, JMS-7401F and Phillips Electron Optics B.V. XL30S FEG, operated at 10 keV) and high-resolution transmission electron microscopy (HR-TEM) (JEOL, Tokyo, Japan, JEM-2200FS), combined with an energy dispersive X-ray spectrometer operated at 200 kV. The elemental compositions and their oxidation states were investigated using X-ray photoelectron spectroscopy (XPS) (Thermo Fisher Scientific, Waltham, MA, USA, ESCALAB 250Xi) and the binding energy of each element was calibrated with respect to the carbon 1s peak at 284.8 eV. The absorbance of photoelectrodes was examined using UV-Vis diffuse reflectance spectroscopy (UV-Vis DRS) (Shimadzu, Kyoto, Japan, UV2501PC).

2.4. Photoelectrochemical Measurements

All photoelectrochemical CO₂ reduction experiments (J-V, J-t, and EIS) were conducted in a three electrodes configuration with ZnTe-based working electrodes, a graphite rod counter electrode, and an Ag/AgCl (4 M KCl) reference electrode, under simulated solar illumination in an undivided gas-tight cell. Simulated solar illumination was generated using a 300 W Xe lamp (Newport, CA, USA, Oriel, 91-160,) with an AM 1.5 G and an IR filter. The light intensity of 100 mW/cm² was calibrated using the guaranteed reference by National Renewable Energy Laboratories, US. A potentiostat (Gramry, Warminster, PA, USA, Reference 600TM) supplied bias to adjust the potential difference to electrodes connected in a circuit. The exposed comparable illuminating area (0.25–0.3 cm² for J-V measurements and 1–1.2 cm² for J-t measurements) of the photocathodes was masked with insulating epoxy. CO₂-saturated 0.5 M KHCO₃ (Junsei chemicals, Tokyo, Japan) in water was used as the electrolyte.

J-V measurements were performed while cathodically sweeping the potentials at a scan rate of 10 mV/s. J-t measurements were recorded for 3 h at −0.11 V and −0.3 V with respect to RHE. While performing J-t measurements, the produced gases were analyzed using gas chromatography (Agilent, Santa Clara, CA, USA, Model 7890) with a Carboxen 1000 packed column and a thermal conductivity detector for gaseous products—H₂, CO, CO₂, and CH₄. Electrochemical impedance spectroscopy (EIS) measurements were taken at a constant DC potential of −0.11 V vs RHE and an AC potential frequency range of 0.1–100,000 Hz with a 20 mV amplitude.

The faradaic efficiency (FE) is determined by dividing the number of charges used to produce the detected number of products, H₂ or CO, by the total charge passed during the photoelectrochemical measurement using the following equation, where n is the number of electrons required to produce one H₂ or CO molecule, which is 2, and F is Faraday's constant (96485.33 C/mol).

$$\text{FE (\%)} = (n \times \text{mol of product} \times F) / (\text{Total charge passed}) \times 100$$

3. Results and Discussion

3.1. Synthesis of Al:ZnTe Nanorod Photocathodes

The Al-doped ZnTe (Al:ZnTe) nanorod photocathodes used in this work were prepared using a two-step, modified hydrothermal method and following the ion exchange reaction. The preparation method is depicted in the schematic diagram (Scheme S1, SI). The Al-doped ZnO (Al:ZnO) nanorods were hydrothermally grown on the FTO with Al-dopant concentrations in the range of 0–5 at% compared with the concentration of Zn precursors. The Al:ZnO nanorods served as an in situ template and precursors to prepare Al:ZnTe. As the solubility product constant (K_{sp}) for ZnTe (5.0×10^{-34}) is significantly lower than that for ZnO (6.8×10^{-34}), ZnO nanorods were transformed to ZnTe by spontaneous anion exchange reactions and thus ZnO core-ZnTe shell heterojunction type electrode was prepared [21].

ZnTe nanorods with different concentrations of Al dopants (Al:ZnTe X, where X = 0, 1, 3, and 5 represent the at% of Al compared with Zn) were prepared and their photoelectrochemical performance was investigated in Figure S1 in SI. Among the photocathodes, Al:ZnTe 3, containing 3 at% Al dopant, exhibited the highest photocurrent densities. The optimized Al:ZnTe 3 photocathodes were named Al:ZnTe and their physicochemical characteristics and photoelectrochemical activities were compared with those of pristine ZnTe photocathodes.

The XRD patterns of ZnTe and Al:ZnTe showed hexagonal wurtzite ZnO (JCPDS no. 01-089-0511) and zinc blend ZnTe (JCPDS no. 01-065-0385) (Figure 1a). All prepared photocathodes showed two patterns of ZnTe and ZnO, regardless of the Al dopant concentration (Figure S2, SI). Furthermore, neither peak splitting nor shifting was observed by Al doping. Moreover, no crystal structure change occurred by Al doping.

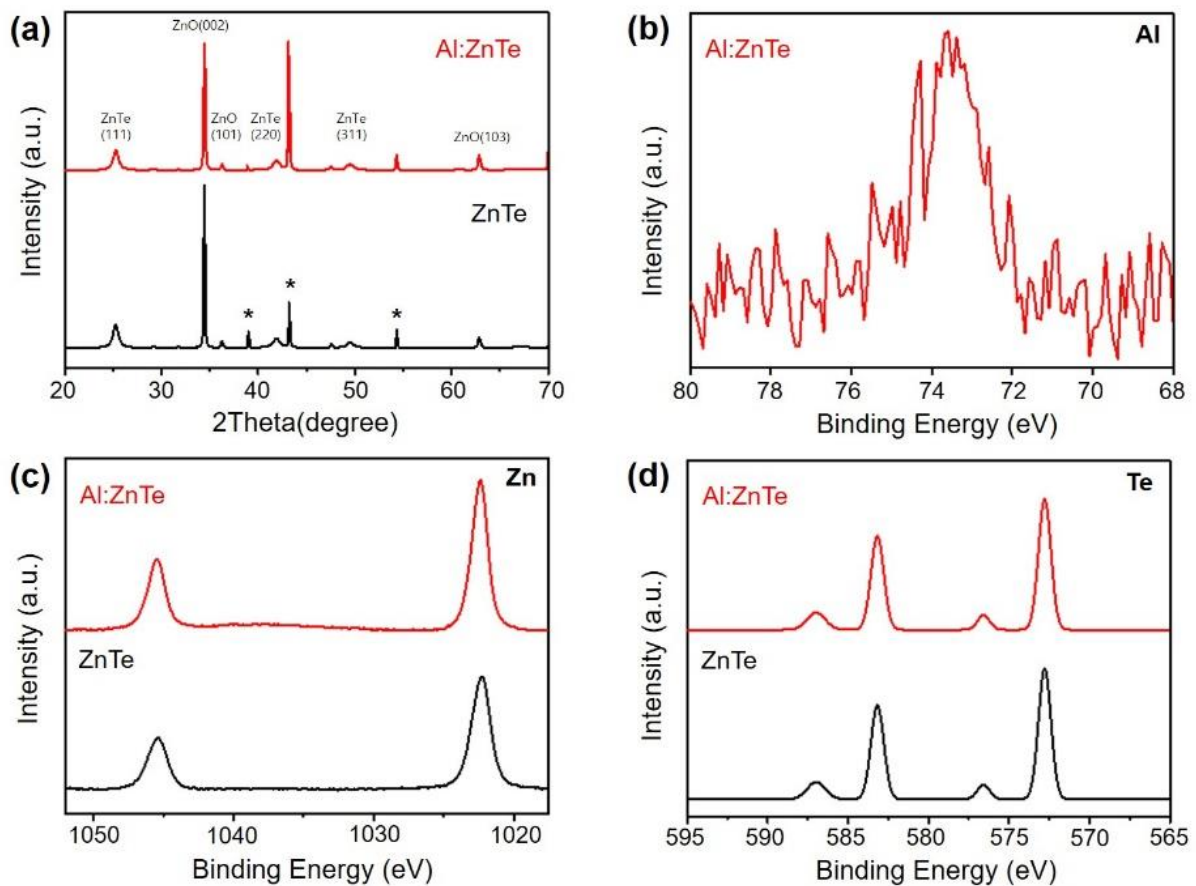


Figure 1. (a) XRD patterns, and XPS spectra for (b) Al 2p, (c) Zn 2p, and (d) Te 4f of Al:ZnTe and ZnTe. * indicates XRD patterns of FTO substrates.

The presence of Al^{3+} in Al:ZnTe was confirmed by the XPS results for the Al 2p orbital (Figure 1b). Additionally, the oxidation states of Zn and Te elements were analyzed to investigate physicochemical changes for ZnTe by Al doping. In the core level of the Zn 2p spectra, two peaks attributed to Zn^{2+} from ZnO and ZnTe slightly positive shifted 0.5 eV by doping with the electron-deficient Al^{3+} relative to Zn^{2+} . However, no significant peak shifts were observed in the core level of the Te 3d results (Figure 1c,d) [22].

Another distinct difference in the morphologies for ZnO and ZnTe resulting from Al doping was observed. The pristine ZnO had a cylindrical nanorod, whereas Al:ZnO had a needle-shaped nanorod (Figure 2a,c). As the concentration of Al dopants increased, the shape transition became more apparent (Figure S3 in SI). The Al:ZnO nanorods were formed by hydrothermal growth of Zn hydroxyl anions with substitutional doping of Al hydroxyl anions. The different valence states and sizes of the two anions induced unique needle shapes for Al:ZnO [23]. Both ZnO and Al:ZnO nanorods were spontaneously transformed to ZnTe and Al:ZnTe via Te^{2-} anion exchange reactions. The radii of ZnTe and Al:ZnTe became larger than those of ZnO and Al:ZnO, respectively, preserving the densities of nanorods in each film (Figure 2b,d). HR-TEM revealed the formation of ZnTe with a lattice spacing of 0.351 nm for zinc blend ZnTe(111) at the outer part of the nanorods (Figure 2e,f).

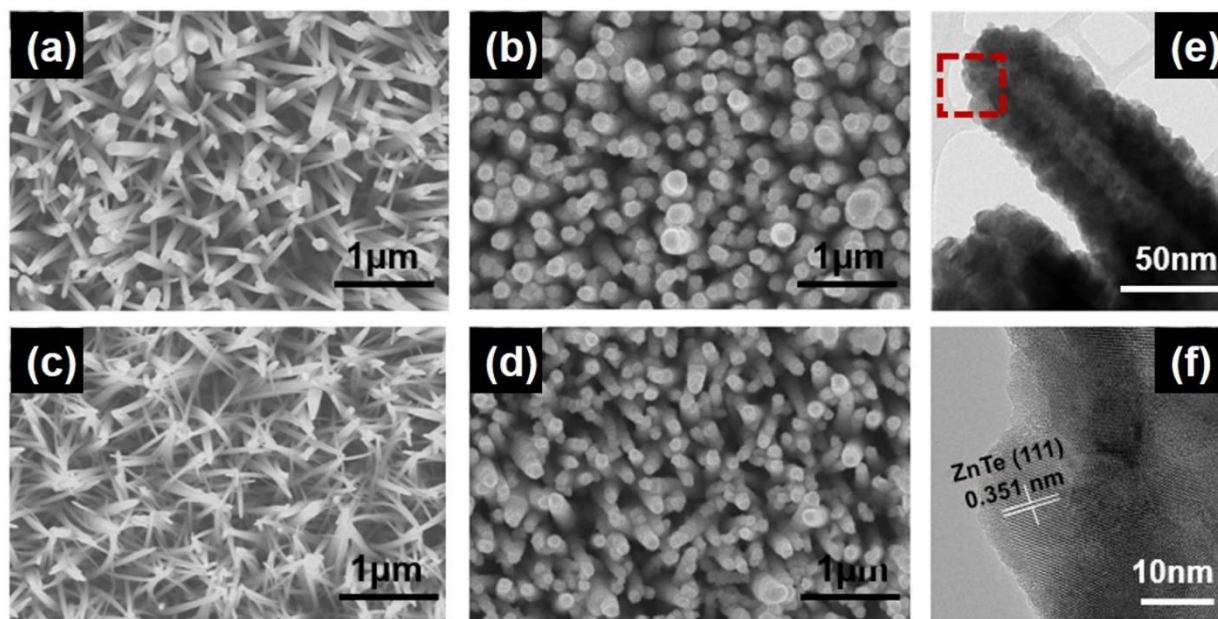


Figure 2. SEM images for (a) ZnO, (b) ZnTe, (c) Al:ZnO, and (d) Al:ZnTe. (e) HR-TEM results for Al:ZnTe, and (f) the magnified view of the region within the red box in (e).

3.2. Photoelectrocatalytic Syngas Production Using Al:ZnTe Nanorod Photocathode

Photoelectrochemical CO₂ reductions were investigated in a conventional three-electrode configuration, using the developed ZnTe-based electrode as a working electrode, an Ag/AgCl reference electrode, and a graphite rod counter electrode, under simulated solar illumination (AM 1.5 G, 100 mW/cm²). To estimate the activity under dark and light conditions simultaneously, the photocurrent-potential (J-V) was measured under chopped illumination in a CO₂-saturated KHCO₃ electrolyte (Figure 3a). The photovoltage gain for CO₂-to-CO reduction, the difference between the photocurrent onset potential ($E_{\text{onset}} - E^{\circ}_{\text{CO}_2/\text{CO}}$) were clearly observed at more than 0.4 V for both ZnTe and Al:ZnTe. For the photocurrent density at the theoretical CO₂/CO redox potential ($E^{\circ}_{\text{CO}_2/\text{CO}}$), $-0.11 V_{\text{RHE}}$ of the Al:ZnTe photocathode exhibited -1.1 mA/cm^2 , which was at least 3.5 times higher than that of the ZnTe photocathode. In the potential range of -0.4 to $0.3 V_{\text{RHE}}$, the Al:ZnTe photocathode exhibited enhanced photocurrent densities compared to the ZnTe photocathode.

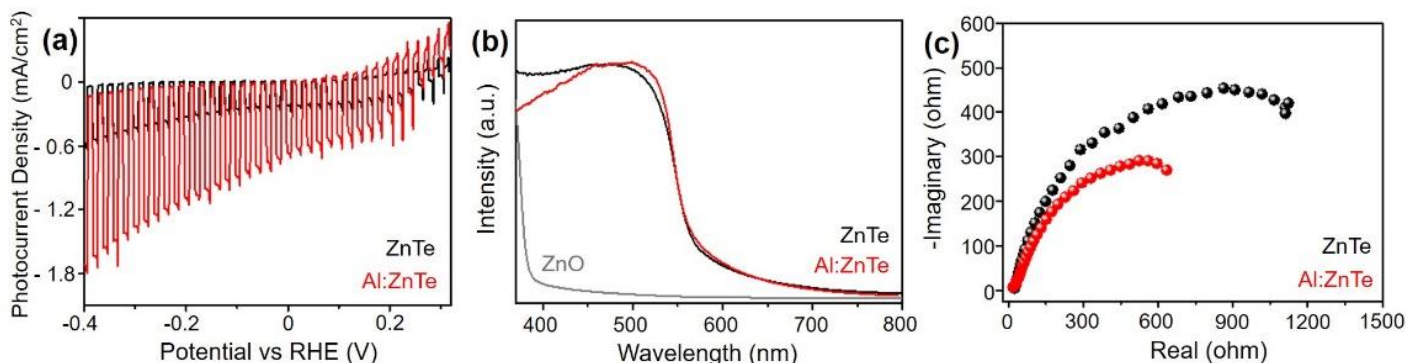


Figure 3. (a) J-V plot (scan rate of 5 mV/s), (b) absorbance, and (c) Nyquist plot of Al:ZnTe and ZnTe. All photoelectrochemical measurements were performed in 0.5 M CO₂-saturated KHCO₃ under simulated solar illumination (AM 1.5 G, 100 mW/cm²). The Nyquist plots were prepared by measuring electrochemical impedance spectroscopy at $-0.11 V_{\text{RHE}}$.

Let us consider the critical origin of the improvement of photocurrent densities due to Al doping on ZnTe. The first possibility is the enhancement of the number of photo-excited carriers resulting from the improvement of the light absorption properties of Al:ZnTe compared to ZnTe [24–27]. However, the light absorbance of Al:ZnTe was approximately similar (330–800 nm) to that of ZnTe. (Figure 3b) Considering the direct bandgap of Al:ZnTe (2.26 ± 0.02 eV) and ZnTe (2.24 ± 0.03 eV) determined by Kubelka-Munk relation using their absorbance, Al doping strategy had a negligible effect to increase the number of photo-generated carriers.

Another possibility is the enhancement of photo-excited carrier separation due to Al doping, resulting from the decrease of resistance to charge transfer [28–30]. The Nyquist plots, prepared by measuring EIS, show that Al:ZnTe has a smaller semicircular radius than ZnTe [31] (Figure 3c). As the radius in the Nyquist plots corresponds to the impedance value, it indicates that Al:ZnTe has a relatively reduced impedance and improved charge transfer ability compared to pristine ZnTe. Therefore, the increased majority carriers and surface area by substitutional Al doping are considered to be the two main origins of photocurrent enhancement.

To investigate the product distributions, photoelectrochemical CO₂ reduction was performed on the photocathodes at -0.11 V_{RHE} which is thermodynamic CO₂/CO redox potential. The ZnTe-based photocathodes produced H₂ and CO via two-electron transfer using protons or dissolved CO₂ in the electrolyte, but no additional byproduct was detected (Figure 4). The total product amounts, the sum of H₂ and CO, of the Al:ZnTe photocathode were at least three times higher than those for ZnTe, which perfectly corresponded to increased photocurrents almost three times because of Al doping on ZnTe (Figure 3a).

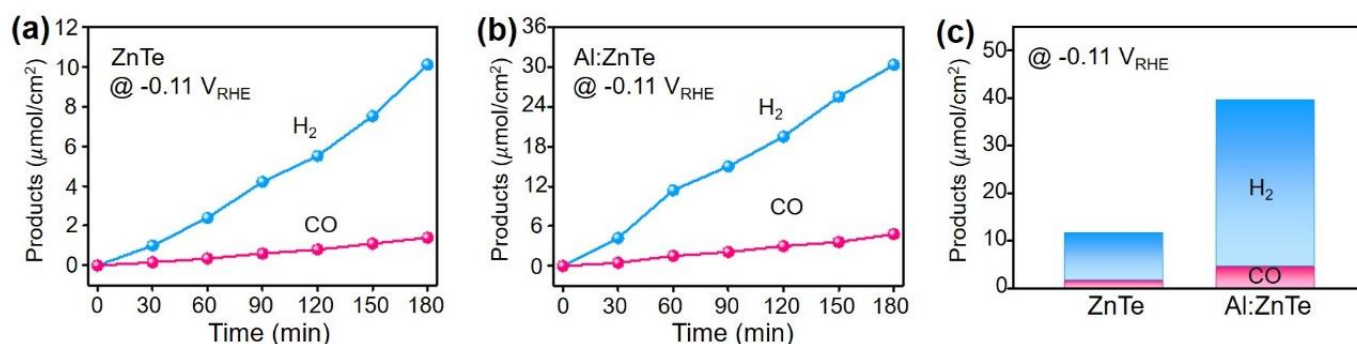


Figure 4. Time profiled products (H₂ and CO) distribution using (a) ZnTe and (b) Al:ZnTe. (c) Comparison plot for accumulated products at -0.11 V_{RHE} measured for 3 h.

Furthermore, to investigate selectivity change resulting from Al doping, the ratio of H₂/CO was compared using data collected from product distributions at -0.11 V_{RHE} (Figure 4c). ZnTe had a ratio of 5.2, whereas Al:ZnTe had a ratio of 5.0. The close ratio values indicate that the H₂ production reaction is approximately five times more favorable than the CO₂-to-CO reduction reaction on the surface of photoelectrodes for both ZnTe and Al:ZnTe as reported previously [16,17]. This suggests that both photoelectrodes provide an identical catalytic nature for electrochemical reactions and that Al dopants were ineffective in altering favorable catalytic reactions.

To further study the possibility of switching major products during photoelectrochemical CO₂ reduction, surface modification using Au electrocatalysts on Al:ZnTe (Al:ZnTe-Au) was conducted. The Au nanoparticles were physically deposited using an E-Beam evaporator and their atomic ratio was approximately 1% [13]. The J-V curve of Al:ZnTe-Au was identical to that of Al:ZnTe, indicating that the electron transfer rate remained unchanged after Au deposition (Figure 5a).

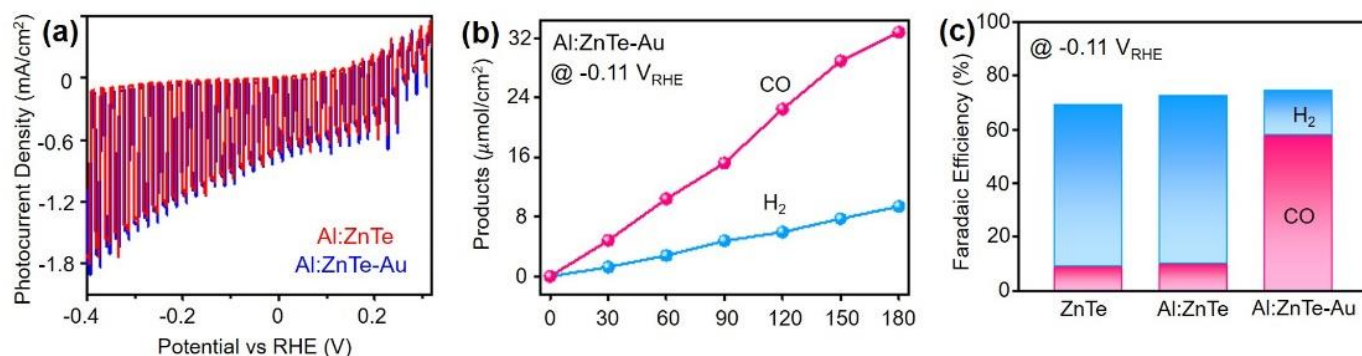


Figure 5. (a) J-V plot (scan rate of 5 mW/s) of Al:ZnTe and Al:ZnTe-Au. (b) Time-profiled product distribution. (c) Faradaic efficiency of each product of H₂ and CO for ZnTe, Al:ZnTe, and Al:ZnTe/Au photocathodes at $-0.11 V_{RHE}$.

In addition, to investigate product distribution differences due to Au coupling, the Al:ZnTe-Au photocathode underwent potential constant photoelectrolysis at $-0.11 V_{RHE}$ and faradaic efficiencies for CO and H₂ were determined based on the quantification results (Figure 5b,c). The imperfect total faradaic efficiencies observed for all ZnTe based photocathode are mainly due to the instability of ZnTe in an aqueous solution [16]. Al:ZnTe-Au exhibited dominant CO production, with $FE_{CO} = 60\%$ and minor H₂ production with $FE_{H_2} = 15\%$. By contrast, Al:ZnTe showed limited CO production ($FE_{CO} = 12\%$) with robust H₂ evolution (60%). The Au nanoparticles can provide active sites for CO production and suppress H₂ production owing to their intrinsically superior electronic nature for CO₂ adsorption, CO₂-to-CO conversion, and CO desorption using transferred protons and electrons, resulting in the major product switch [32–34]. The results demonstrate the availability of photoelectrochemical syngas production. Furthermore, the composition of the syngas—H₂/CO—can be altered by modifying the light absorber using an electrocatalyst.

4. Conclusions

Photoelectrochemical systems can provide an ideal method for direct syngas production via simultaneous CO₂ and water reduction at ambient temperatures and pressures. This provides an alternative to the conventional process, requiring fossil fuels and natural gases at high temperatures and pressures. In this study, highly advanced Al-doped ZnTe nanorod photocathodes (Al:ZnTe) were developed for solar-energy-driven syngas production. This system has the following advantages: (1) a cost-effective solution process to prepare samples, (2) a nanorod array for facilitating photo-excited carrier separation, and (3) substitutional in situ Al doping on the site Zn while hydrothermally growing ZnO NW. Furthermore, a simple strategy was proposed for switching the major product to CO by suppressing competitive H₂ evolution. Au electrocatalyst coupling can provide active sites for CO production. By the combination of all modifications, the advanced Al:ZnTe-Au photocathode represented -1.1 mA/cm^2 at $-0.11 V_{RHE}$ and the ratio of the H₂:CO to 1:4, whereas pristine ZnTe exhibited -0.31 mA/cm^2 with the syngas production ratio to 5:1. With further research advances, the developed system can be applied for solar-driven value-added chemicals production in practical.

Supplementary Materials: The following supporting information can be downloaded at: <https://www.mdpi.com/article/10.3390/ma15093102/s1>, Scheme S1: Schematic diagram for synthesis, Figure S1: J-V plots, Figure S2: XRD patterns, Figure S3: SEM images.

Author Contributions: Investigation, reproducibility tests, and writing by C.L., Y.H.M. and S.C.; conceptualization, experiments, writing/editing, supervision, and funding acquisition by Y.J.J. All authors have read and agreed to the published version of the manuscript.

Funding: This research was supported by the National Research Foundation of Korea (NRF) grant (No. 2021R1A4A3027878), the Korea Institute of Energy Technology Evaluation and Planning

(KETEP), and the Ministry of Trade, Industry & Energy (MOTIE) (No. 20202020800330), and the Graduate School of Post Plastic Specialization of Korea Environmental Industry & Technology Institute grant funded by the Ministry of Environment of the Republic of Korea.

Institutional Review Board Statement: Not applicable.

Informed Consent Statement: Not applicable.

Data Availability Statement: The data presented in this study are available upon request from the corresponding author.

Conflicts of Interest: The authors declare no conflict of interest.

References

1. Mahmoudi, H.; Mahmoudi, M.; Doustdar, O.; Jahangiri, H.; Tsolakis, A.; Gu, S.; Wyszynski, M.L. A review of Fischer Tropsch Synthesis Process, Mechanism, Surface Chemistry and Catalyst Formulation. *Biofuels Eng.* **2017**, *2*, 11–31. [[CrossRef](#)]
2. Gholami, Z.; Tisler, Z.; Rubas, V. Recent advances in Fischer-Tropsch Synthesis Using Cobalt-Based Catalysts: A Review on Supports, Promoters, and Reactors. *Catal. Rev.* **2021**, *63*, 512–595. [[CrossRef](#)]
3. Zhao, K.; Chen, J.; Li, H.; Zheng, A.; He, F. Effects of Co-substitution on the reactivity of double perovskite oxides $\text{LaSrFe}_{2-x}\text{Co}_x\text{O}_6$ for the chemical-looping steam methane reforming. *J. Energy Inst.* **2019**, *92*, 594–603. [[CrossRef](#)]
4. Bai, Y.; Wang, Y.; Yuan, W.; Sun, W.; Zhang, G.; Zheng, L.; Han, X.; Zhou, L. Catalytic performance of perovskite-like oxide doped cerium ($\text{La}_{2-x}\text{Ce}_x\text{CoO}_{4\pm y}$) as catalysts for dry reforming of methane. *Chin. J. Chem. Eng.* **2019**, *27*, 379–385. [[CrossRef](#)]
5. Chu, S.; Ou, P.; Ghamari, P.; Vanka, S.; Zhou, B.; Shih, I.; Song, J.; Mi, Z. Photoelectrochemical CO_2 Reduction into Syngas with the Metal/Oxide Interface. *J. Am. Chem. Soc.* **2018**, *140*, 7869–7877. [[CrossRef](#)]
6. Vesborg, P.C.K.; Seger, B. Performance Limits of Photoelectrochemical CO_2 Reduction Based on Known Electrocatalysts and the Case for Two-Electron Reduction Products. *Chem. Mat.* **2016**, *28*, 8844–8850. [[CrossRef](#)]
7. Jang, Y.J.; Lindberg, A.E.; Lumley, M.A.; Choi, K.-S. Photoelectrochemical Nitrogen Reduction to Ammonia on Cupric and Cuprous Oxide Photocathodes. *ACS Energy Lett.* **2020**, *5*, 1834–1839. [[CrossRef](#)]
8. Jang, Y.J.; Lee, J.S. Photoelectrochemical Water Splitting with p-Type Metal Oxide Semiconductor Photocathodes. *ChemSusChem* **2019**, *12*, 1835–1845. [[CrossRef](#)] [[PubMed](#)]
9. Lumley, M.A.; Radmilovic, A.; Jang, Y.J.; Lindberg, A.E.; Choi, K.-S. Perspectives on the Development of Oxide-Based Photocathodes for Solar Fuel Production. *J. Am. Chem. Soc.* **2019**, *141*, 18358–18369. [[CrossRef](#)] [[PubMed](#)]
10. Jang, J.-W.; Cho, S.; Magesh, G.; Jang, Y.J.; Kim, J.Y.; Kim, W.Y.; Seo, J.K.; Kim, S.; Lee, K.-H.; Lee, J.S. Aqueous-Solution Route to Zinc Telluride Films for Application to CO_2 Reduction. *Angew. Chem.-Int. Edit.* **2014**, *53*, 5852–5857. [[CrossRef](#)] [[PubMed](#)]
11. Jang, Y.J.; Lee, J.; Kim, J.H.; Lee, B.J.; Lee, J.S. One-dimensional CuIn alloy nanowires as a robust and efficient electrocatalyst for selective CO_2 -to-CO conversion. *J. Power Sources* **2018**, *378*, 412–417. [[CrossRef](#)]
12. Liu, A.; Gao, M.; Ren, X.; Meng, F.; Yang, Y.; Gao, L.; Yang, Q.; Ma, T. Current Progress in Electrocatalytic Carbon Dioxide Reduction to Fuels on Heterogeneous Catalysts. *J. Mater. Chem. A* **2020**, *8*, 3541–3562. [[CrossRef](#)]
13. Jang, Y.J.; Jang, J.-W.; Lee, J.; Kim, J.H.; Kumagai, H.; Lee, J.; Minegishi, T.; Kubota, J.; Domen, K.; Lee, J.S. Selective CO production by Au coupled ZnTe/ZnO in the photoelectrochemical CO_2 reduction system. *Energy Environ. Sci.* **2015**, *8*, 3597–3604. [[CrossRef](#)]
14. Foit, S.R.; Vinke, I.C.; de Haart, L.G.J.; Eichel, R.-A. Power-to-Syngas: An Enabling Technology for the Transition of the Energy System? *Angew. Chem.-Int. Edit.* **2017**, *56*, 5402–5411. [[CrossRef](#)] [[PubMed](#)]
15. Hernández, S.; Amin Farkhondeh, M.; Sastre, F.; Makkee, M.; Saracco, G.; Russo, N. Syngas production from electrochemical reduction of CO_2 : Current status and prospective implementation. *Green Chem.* **2017**, *19*, 2326–2346. [[CrossRef](#)]
16. Jang, Y.J.; Bhatt, M.D.; Lee, J.; Choi, S.H.; Lee, B.J.; Lee, J.S. Metal-Free Artificial Photosynthesis of Carbon Monoxide Using N-Doped ZnTe Nanorod Photocathode Decorated with N-Doped Carbon Electrocatalyst Layer. *Adv. Energy Mater.* **2018**, *8*, 1702636. [[CrossRef](#)]
17. Jang, Y.J.; Jeong, I.; Lee, J.; Ko, M.J.; Lee, J.S. Unbiased Sunlight-Driven Artificial Photosynthesis of Carbon Monoxide from CO_2 Using a ZnTe-Based Photocathode and a Perovskite Solar Cell in Tandem. *ACS Nano* **2016**, *10*, 6980–6987. [[CrossRef](#)]
18. Won, D.H.; Chung, J.; Park, S.H.; Kim, E.-H.; Woo, S.I. Photoelectrochemical production of useful fuels from carbon dioxide on a polypyrrole-coated p-ZnTe photocathode under visible light irradiation. *J. Mater. Chem. A* **2015**, *3*, 1089–1095. [[CrossRef](#)]
19. Boubenia, S.; Dahiya, A.S.; Poulin-Vittrant, G.; Morini, F.; Nadaud, K.; Alquier, D. A facile hydrothermal approach for the density tunable growth of ZnO nanowires and their electrical characterizations. *Sci. Rep.* **2017**, *7*, 15187. [[CrossRef](#)] [[PubMed](#)]
20. Liu, J.; Xu, L.; Wei, B.; Lv, W.; Gao, H.; Zhang, X. One-step hydrothermal synthesis and optical properties of aluminium doped ZnO hexagonal nanoplates on a zinc substrate. *CrystEngComm* **2011**, *13*, 1283–1286. [[CrossRef](#)]
21. Clever, H.L.; Derrick, M.E.; Johnson, S.A. The Solubility of Some Sparingly Soluble Salts of Zinc and Cadmium in Water and in Aqueous Electrolyte Solutions. *J. Phys. Chem. Ref. Data* **1992**, *21*, 941–1004. [[CrossRef](#)]
22. Bai, S.; Guo, T.; Zhao, Y.; Luo, R.; Li, D.; Chen, A.; Liu, C.C. Mechanism enhancing gas sensing and first-principle calculations of Al-doped ZnO nanostructures. *J. Mater. Chem. A* **2013**, *1*, 11335–11342. [[CrossRef](#)]
23. Cho, S.; Jung, S.-H.; Jang, J.-W.; Oh, E.; Lee, K.-H. Simultaneous Synthesis of Al-Doped ZnO Nanoneedles and Zinc Aluminum Hydroxides through Use of a Seed Layer. *Cryst. Growth Des.* **2008**, *8*, 4553–4558. [[CrossRef](#)]

24. White, J.L.; Baruch, M.F.; Pander, J.E.; Hu, Y.; Fortmeyer, I.C.; Park, J.E.; Zhang, T.; Liao, K.; Gu, J.; Yan, Y.; et al. Light-Driven Heterogeneous Reduction of Carbon Dioxide: Photocatalysts and Photoelectrodes. *Chem. Rev.* **2015**, *115*, 12888–12935. [[CrossRef](#)]
25. Choi, M.; Lee, J.H.; Jang, Y.J.; Kim, D.; Lee, J.S.; Jang, H.M.; Yong, K. Hydrogen-doped Brookite TiO₂ Nanobullets Array as a Novel Photoanode for Efficient Solar Water Splitting. *Sci. Rep.* **2016**, *6*, 36099. [[CrossRef](#)] [[PubMed](#)]
26. Parmar, K.P.S.; Kang, H.J.; Bist, A.; Dua, P.; Jang, J.S.; Lee, J.S. Photocatalytic and Photoelectrochemical Water Oxidation over Metal-Doped Monoclinic BiVO₄ Photoanodes. *ChemSusChem* **2012**, *5*, 1926–1934. [[CrossRef](#)]
27. Jo Won, J.; Kang Hyun, J.; Kong, K.-J.; Lee Yun, S.; Park, H.; Lee, Y.; Buonassisi, T.; Gleason Karen, K.; Lee Jae, S. Phase transition-induced band edge engineering of BiVO₄ to split pure water under visible light. *Proc. Natl. Acad. Sci. USA* **2015**, *112*, 13774–13778.
28. Li, S.; Jiang, Y.; Wu, D.; Wang, L.; Zhong, H.; Wu, B.; Lan, X.; Yu, Y.; Wang, Z.; Jie, J. Enhanced p-Type Conductivity of ZnTe Nanoribbons by Nitrogen Doping. *J. Phys. Chem. C* **2010**, *114*, 7980–7985. [[CrossRef](#)]
29. Rakhshani, A.E.; Thomas, S. Nitrogen doping of ZnTe for the preparation of ZnTe/ZnO light-emitting diode. *J. Mater. Sci.* **2013**, *48*, 6386–6392. [[CrossRef](#)]
30. Zhang, L.; Liu, C.; Yang, Q.; Cui, L.; Zeng, Y. Growth and characterization of highly nitrogen doped ZnTe films on GaAs (001) by molecular beam epitaxy. *Mater. Sci. Semicond. Process* **2015**, *29*, 351–356. [[CrossRef](#)]
31. Jang, Y.J.; Lee, J.; Lee, J.; Lee, J.S. Solar Hydrogen Production from Zinc Telluride Photocathode Modified with Carbon and Molybdenum Sulfide. *ACS Appl. Mater. Interfaces* **2016**, *8*, 7748–7755. [[CrossRef](#)] [[PubMed](#)]
32. Hori, Y.; Wakebe, H.; Tsukamoto, T.; Koga, O. Electrocatalytic process of CO selectivity in electrochemical reduction of CO₂ at metal electrodes in aqueous media. *Electrochim. Acta* **1994**, *39*, 1833–1839. [[CrossRef](#)]
33. Zhang, L.; Zhu, D.; Nathanson, G.M.; Hamers, R.J. Selective Photoelectrochemical Reduction of Aqueous CO₂ to CO by Solvated Electrons. *Angew. Chem.-Int. Ed.* **2014**, *53*, 9746–9750. [[CrossRef](#)]
34. Nitopi, S.; Bertheussen, E.; Scott, S.B.; Liu, X.; Engstfeld, A.K.; Seger, B.; Stephens, I.E.L.; Chan, K.; Hahn, C.; Norskov, J.K.; et al. Progress and Perspective of Electrochemical CO₂ Reduction on Copper in Aqueous Electrolyte. *Chem. Rev.* **2019**, *119*, 7610–7672. [[CrossRef](#)]